Modelling global offshore turbulence intensity including large-scale turbulence, stability and sea state

Xiaoli Guo Larsén[1], Marc Imberger[1], and Rogier Floors[1]

[1]Wind and Energy Systems Department, Technical University of Denmark, Frederiksborgvej 399, Roskilde, 4000, Denmark

Correspondence: Xiaoli Guo Larsén (xgal@dtu.dk)

Abstract. This study delivers a method and datasets for a global offshore atlas for turbulence intensity (TI) from 10 m to 200 m. The method includes both surface driven, three dimensional boundary-layer turbulence, and large-scale two-dimensional turbulence. This systematically includes the effect of large scale eddies, particularly at weak wind conditions, and hence significantly improves TI in weak to moderate wind conditions. This method describes water roughness length through a dependence on wave age and wind speed, which is suitable for moderate to strong wind conditions. The method also includes stability dependence through the Obukhov length. Based on theories and measurements in literature, algorithms for TI have been calibrated for heights up to 200 m. We use the ERA5 atmospheric and wave data to demonstrate the use of the method and create a global dataset. The results show satisfactory agreement with measurements and data from the literature.

1 Introduction

Turbulence Intensity (TI) is one of the most used parameters in wind energy. For example, it is needed to make decisions about the turbine class for a particular place as required by the IEC-61400 standard (IEC, 2019). It is required to calculate loads and fatigue. It is also an input parameter for engineering wake modeling.

The most direct way to obtain TI is through wind speed measurements from which the standard deviation and the mean are calculated during a given period T. For wind speed close to the ground, T is typically 10 min to 1 h. Cup anemometers, lidar and sonic anemometers are often used to measure TI, with sonic anemometers usually providing the most reliable turbulence data due to their fast response to flow fluctuations, but they are also the most expensive.

Measurements are generally expensive to collect, particularly for offshore conditions due to costs related to, e.g., operation, maintenance, and data transfer. Traditionally, met-mast or LIDAR are installed to measure the wind conditions for e.g., a year or more, before the wind farm is being built. With the rapid and large-scale development of offshore wind energy, there is often limited time to take such measurements, and therefore the information on TI relies heavily on modeling.

In the lack of measurements, TI needs to be modeled. The Global Atlas for Siting Parameters (GASP) project (Larsén et al., 2022) provided a near global, modeled dataset of TI at a spatial grid spacing of 275 m from a height of 10 m to 150 m. This dataset includes both land and water areas, with water areas reaching 200 km from coastlines, leaving most of open ocean excluded. The calculation of TI over water used the mean wind statistics from ERA5 data as input to the Kaimal turbulence model (Kaimal et al., 1972), with the surface roughness length z_0 described through the Charnock formulation. The dataset has

been applied in the GASP project for defining turbine classes and thus only the moderate to strong wind ranges were used and validated.

This study aims to improve the methodology and data sets for TI for offshore conditions from the GASP project, covering all global offshore areas, addressing also low to moderate winds in addition to moderate to strong wind conditions as in GASP.

30 For offshore conditions, the IEC (2019) standard suggests a simple monotonic decrease of TI with wind speed U, without dependence on height:

$$TI_{IEC} = I_{ref}(0.75 + \frac{5.6}{U}), \tag{1}$$

where 5.6 is in ms^{-1}. Eq. 1 is obviously only valid over land, because over water it is expected that the surface becomes rougher as the winds increase, contributing to the higher intensity of turbulence in stronger winds, which is supported by measurements 35 (Wang et al., 2014; Christakos et al., 2016; Jeans, 2024).

Wang et al. (2014) developed algorithms from boundary-layer surface scaling laws, where TI is a function of stability and boundary-layer height (z_i), and depends on roughness length z_0 and surface momentum and heat fluxes. To take into account the wave effect, they used the Charnock formulation for the roughness length $z_0 = \alpha_{ch} u_*^2 / g$, where α_{ch} is the Charnock parameter, for which a typical value of 0.011 is taken. Thus, TI increases with wind speed over the water. The details of the 40 equation for TI from Wang et al. (2014) are included in Appendix A (Eq. A1).

The ISO (2015) standard recommends an increase of TI with wind speed and a decrease with height:

$$TI_{ISO} = 0.06(1 + 0.43\frac{U}{10})(\frac{z}{10})^{-0.22}, \tag{2}$$

where U is the wind speed at height z.

Similar relationships between TI and U have also been empirically derived through measurements. Andersen and Løvseth 45 (2006) used measurements from the Frøya site and proposed several similar expressions with U scaled with 10 m s^{-1} and z scaled with 10 m: $(z/10)^{-0.2}$, primarily for the wind speed range from 10 to 26 ms^{-1}. Three such expressions are included in Appendix A (Eqs. A2 to A4).

The expressions from ISO standard, from Wang et al. (2014) and Andersen and Løvseth (2006) do not include the decreasing dependence of TI on wind speed under lower wind speed conditions. Wang et al. (2014) added such a dependence at lower 50 wind speed by imposing climatological unstable stratification, which corresponds to stronger vertical mixing and hence larger turbulence intensity.

This decreasing dependence of TI on U at low wind speeds was considered in Christakos et al. (2016) when deriving an empirical relation based on measurements from the FINO masts:

$$TI_C = c_1 U + c_2 + \frac{c_3}{U}. \tag{3}$$

55 The height dependence of TI is not explicitly included in the expression above, but considered through the set of coefficients c_1, c_2 and c_3. For the FINO cases, two sets of coefficients for each site were derived, for 30 m and 100 m, respectively.

The study of Jeans (2024) could be considered a summary for the above expressions, including the increase of TI with U for moderate to strong winds, and decrease for light winds, and a similar height dependence of TI to the ISO relationship and

the Frøya expressions:

$$TI_{Jeans} = \left(a_1 \frac{U(z)}{10} + a_2 + a_3 \left(\frac{U(z)}{10}\right)^{-1}\right)\left(\frac{z}{10}\right)^{-0.22}, \tag{4}$$

where $a_1 = 0.035$, $a_2 = 0.0089$ and $a_3 = 0.0402$ are the default values. The coefficients a_1, a_2 and a_3 can be tuned to represent site-specific data, and different values for the three coefficients are also provided for different stability conditions. This expression has been validated in Jeans (2024) with data up to 82 m.

In the above-mentioned TI expressions, only the scaling modeling approach from Wang et al. (2014) is based on physics arguments, the others are empirical, driven by fitting to measurement. This has caused a large variety of sets of coefficients to these expressions, depending on the sites and sometimes measurement heights.

With respect to the application of physics, high-fidelity models are sometimes used to calculate turbulence parameters from which TI can be calculated, such as the Large Eddy Simulation (LES). Due to its high computational cost, it can only be used for a very limited area, over a short period, or in idealized settings. Mesoscale modeling outputs, although by design not capable of resolving turbulence, are sometimes post-processed to match expected results, e.g., in Tai et al. (2023).

In this study, we create a global offshore atlas for TI using a new and cost-effective approach that is based on physical principles. First, we model turbulence. Usually, the calculation of turbulence and hence TI considers only surface-driven three-dimensional (3D) turbulence using, for instance, the Kaimal model, the Mann model and the Veers model (Kaimal et al., 1972; Mann, 1994; Veers, 1988). The black dotted curves in Fig. 1 show examples of the wind speed power spectra driven by the 3D turbulence at the site Høvsøre at two heights (refer to Section 2.1 for details of this figure). The Kaimal and Veers models require input of surface information such as z_0 or u_*, and the Mann model requires turbulence spectra (either from measurements or from other models) as input to further calculate the three-dimensional flow. In most cases, these models are used under the assumption of neutral stability. In common, these models (represented by the black curves in Fig. 1) does not include wind fluctuations from the larger-scales (blue curves for frequency f lower than approximately 10^{-3} Hz). With the current offshore wind energy development and deployment, wind farm clusters can be of the size of several hundreds of square kilometers, and the tallest wind turbine has a hub height of about 185 m, reaching a height of 310 m with rotors (26 MW turbine). Including the contribution of large-scale turbulence is necessary and is listed as one of the "Grand Challenges" for the application of wind energy (Kosovic et al., 2025). Thus, this study will take into account the contribution of the large-scale two-dimensional (2D) turbulence, using the full-scale model provided by Larsén et al. (2016). In addition to the 3D and 2D turbulence, our calculation also includes the effect of stability, sea state, and height dependence calibrated up to 200 m. The outcome of the method is a Look-Up Table (LUT). We call the method developed here the "LUT" method.

The output is valuable for an initial evaluation of the cost related to the design of the wind turbine and the wind farm, including the mean characteristics of TI, the 90th-percentile and standard deviation of the TI-standard deviation, σ_σ of TI.

The method and application are demonstrated through the use of modeled data, here the ERA5 reanalysis data (see section 3). The method is introduced in section 2. Results with validations are shown in section 4, followed by discussions and conclusions in sections 5 and 6, respectively.

2 Method for calculation of turbulence intensity

To calculate the turbulence intensity TI, we start with its definition

$$TI = \sigma_U / \overline{U} \tag{5}$$

95   where $\overline{U}$ is the mean wind speed and σ_U is the standard deviation of the wind speed.

In the absence of measured high frequency time series of wind speed, we calculate σ_U by integrating the turbulence spectrum model for the wind speed from a lower cutoff frequency f_1 to a higher cutoff frequency f_2, so:

$$\sigma_U = \left(\int_{f_1}^{f_2} S(f) df \right)^{1/2} \tag{6}$$

where $S(f)$ is the turbulence power spectrum, the modeling of which is introduced in section 2.1. In boundary-layer turbulence, 100 f_1 is a value in the spectral gap, typically $(10 \text{ min})^{-1}$, or $(1 \text{ h})^{-1}$, while f_2 is a value in the inertial dissipation range, e.g. 10 Hz, corresponding to a time series sampled at 20 Hz, typical for sonic measurements.

The following sub-sections explain how both the effects of the typical boundary-layer turbulence (the 3D turbulence) and large-scale variability (the 2D turbulence) are included in the calculation of TI (sections 2.1), how the sea state dependence is introduced through parameterisation of z_0 as a function of wave age c_p/u_* (section 2.2), how the stability effect is included in 105   the algorithms (section 2.3), how the 90th-percentile of TI is calculated (section 2.4) and how the height-dependence is added and calibrated (section 2.5).

These algorithms will then be run by using a set of corresponding parameters defined in specific ranges, thus constructing a final Look-Up Table with broad ranges of wind, wave and stability conditions combined. The set of parameters and their respective ranges are: (1) wind speed at 10 m from 0.1 to 45 m s^{-1}. (2) wave phase velocity at peak frequency c_p from 0.1 to 110   30 m s^{-1}. (3) stability parameter z/L at 10 m from -3 to 3. (4) 12 wind sectors. (5) height $z =$ 10, 50, 100, 150 and 200 m.

For application, at a given site, with input of wind speed at a given height (U_z), wave phase velocity (c_p) and stability (z/L at 10 m), we can find the corresponding TI from the LUT.

In this study we use the open source data the fifth generation ECMWF Reanalysis data (Hersbach et al., 2020), ERA5, to demonstrate how these algorithms can be applied globally; the details and preparation of the ERA5 data are provided in section 115   3.

2.1 Adding large-scale turbulence

As mentioned previously, usually, when calculating variance and thereafter standard deviation and turbulence intensity, one integrates Eq. 6 from $f_1 = (10 \text{ min})^{-1}$ or $f_1 = (1 \text{ h})^{-1}$, to $f_2 = 10$ Hz.

Figure 1 illustrates the concept of the 3D and the 2D turbulence. Data in Fig. 1 are exported from the study Larsén et al. 120   (2016). The blue curves are the mean spectra from one-year sonic anemometer data at 10 m (Fig. 1a) and 100 m (Fig. 1b). The Høvsøre site is located at the west coast of Denmark, where the winds from the west, namely the sea, dominate. The prevailing

winds at 100 m represent the sea condition and that at 10 m is sometimes affected by the underlying land. Over sea, the spectra will resemble more Fig. 1b, where the 3D turbulence is in general rather weak due to smooth water surface, and therefore the relative contribution from 2D turbulence is bigger.

125   The black dotted lines show the typical boundary-layer 3D spectra for wind speed. For $f < f_p$, the Kaimal model shape suggests a saturation of power spectrum at lower frequencies, shown as a 1:1 slope in the plot of $fS(f)$ vs. f in log-log coordinates:

$$fS_{1,u}(f) \quad = \quad \frac{\alpha 102 u_*^2 fz/U}{(1 + 33 fz/U)^{5/3}}. \tag{7}$$

where U is the mean wind speed, and z is the height. $\alpha = 1$ by default. S_1 is for the 3D turbulence.

130   The green dashed curves are the spectral model for large-scale variability from Larsén et al. (2013):

$$fS_{2,u}(f) = a_1 f^{-2/3} + a_2 f^{-2} \tag{8}$$

where $a_1 = 3 \times 10^{-4}$ m^2 s$^{-8/3}$ and $a_2 = 3 \times 10^{-11}$ m^2 s^{-4} are derived from offshore climatological wind data sets. S_2 is for the 2D turbulence.

The red curve is a superposition of the Kaimal model and the large-scale variability from Larsén et al. (2016):

135    $$fS_u(f) = f \cdot \big(S_{1,u}(f) + S_{2,u}(f)\big) \tag{9}$$

The good agreement between the red (model) and blue curves (measurements) suggests the success in bridging the 2D and 3D turbulence calculation using Eq. 9 the full-spectrum model in the gap region.

The scales of 1 h and 10 min are marked in vertical gray lines in Fig. 1. If the integration of Eq. 6 uses the black dotted curves for the 3D turbulence only, using $f_1 = (1 \text{ h})^{-1}$ gives slightly larger variance and hence slightly larger TI than using

140    $f_1 = (10 \text{ min})^{-1}$. The black dotted curves obviously miss out significant amounts of energy for $f < (10 \text{ min})^{-1}$, compared to the blue curves, which are the measurements, and well described by the model Eq. 9, the red curve. In this study, we use the red curve for the integration of the power spectrum, with $f_1 = 1 \text{ h}^{-1}$, and $f_2 = 10$ Hz, thus adding the large-scale turbulence.

2.2   Adding wave effect

The wave effect is added through the roughness length z_0, which is used in the wind profile algorithm:

145    $$U(z) = \frac{u_*}{\kappa} \left[\ln (z/z_0) - \psi_m \right] \tag{10}$$

where ψ_m is the stability function, dependent on the Obukhov length scale $L = -u_*^2 \overline{\theta}/(\kappa g \Theta_*)$, with $\kappa = 0.41$ the Von Kármán constant, $\Theta_* = \overline{w'\theta'}/u_*$, and $\overline{\theta}$ is the mean surface temperature in °K. The details for ψ_m are provided in Section 2.3.

The roughness of the water surface z_0 is related to the sea state, water fetch and water depth.

In this study, we apply the simple sea state dependence, namely the wind sea, and focus on wind-generated waves in open sea

150   conditions. There are many models to describe water roughness z_0 through parameters of the sea state, such as significant wave
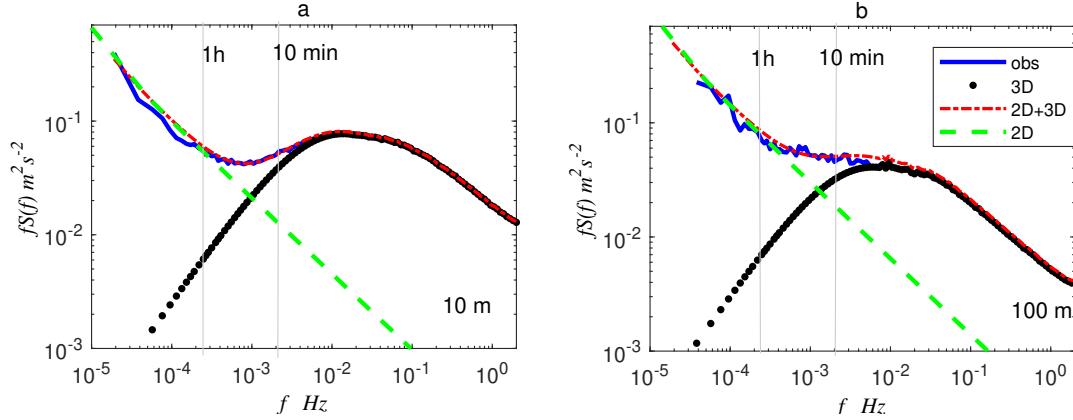
Figure 1. Illustration of the effect of large scale wind variation on the variance from the gap region using data from Høvsøre (Larsén et al., 2016). Power spectra of wind speed at (a) 10 m, and (b) 100 m. The scale of 1 hour and 10 min are marked with thin gray lines. The spectra from the measurements are shown in blue curve, the 3D turbulence for $f < f_p$ is shown as the Kaimal model in black dots (the 3D turbulence for $f > f_p$ is from measurements), and green dashed curve is the mesoscale spectral model from Larsén et al. (2013) (here Eq. 8) and the red dash-dotted curve is the 2D+3D turbulence model.

height, wave length, wave steepness, and wave age; see e.g., Larsén et al. (2019) for a summary. Here we build the sea-state dependence upon the Charnock formulation, with consideration of the smooth water effect for z_0:

$$z_0 = 0.11\nu/u_* + \alpha_{ch}u_*^2/g, \tag{11}$$

The first term on the right-hand side is the smooth flow effect due to viscosity, with ν the viscosity coefficient; it introduces a
155   weak decrease of z_0 with increasing wind speed for light wind conditions. The viscosity effect becomes negligible at moderate to strong winds. For the second term in Eq. 11, we use the parameterization scheme from Fan et al. (2016) through wave age c_p/u_* in connection with the Charnock parameter

$$\alpha_{ch} = a(c_p/u_*)^b, \tag{12}$$

where $a = 0.023/1.0568^{U_{10}}$ and $b = 0.012U_{10}$, with U_{10} the wind speed at 10 m. The reason for choosing the Fan-scheme is
160   based on the study of Larsén et al. (2019), in which they compared six parameterization schemes with measurements at the Horns Rev site where the Fan-scheme provides the calculation of z_0 closest to the measurements.

To calculate u_* for Eqs. 11 and 12, we used the bulk air-sea surface flux algorithms developed in Andreas et al. (2015):

$$u_* = 0.239 + 0.0433\left((U_{10} - 8.271) + \sqrt{0.12(U_{10} - 8.271)^2 + 0.181}\right). \tag{13}$$

The wave phase velocity at the peak frequency c_p is calculated through the wave dispersion relation through the peak wave
165   number k_p, considering the water depth h:

$$c_p = \sqrt{\frac{g}{k_p}\tanh(k_p h)}. \tag{14}$$

2.3 Adding stability effect

Atmospheric stability is introduced in the calculation through the wind speed profile (Eq. 10). For stable condition, $z/L > 0$, we used:

$$\psi_m = -5z/L, \tag{15}$$

and for unstable condition, $z/L < 0$, we used:

$$\psi_m = \ln\left(\frac{1}{2}(1+X^2)(\frac{1+X}{2})^2\right) - 2\arctan(X) + \frac{\pi}{2} \tag{16}$$

where

$$X = (1 - 15z/L)^{1/4} \tag{17}$$

There are many recommendations in the literature on the coefficients that are used together with the stability parameter z/L in Eqs. 15 and 16, see a summary in Högström (1996).

For neutral conditions, $\psi_m = 0$, and $U = U_N$, where

$$U_N(z) = \frac{u_*}{\kappa}\ln(z/z_0). \tag{18}$$

Thus the relationship between TI and turbulence intensity for the neutral condition, TI_N, can be derived through Eqs. 10 and 18 accordingly:

$$TI = TI_N \cdot \frac{\ln(z/z_0)}{\ln(z/z_0) - \psi_m}. \tag{19}$$

2.4 Adding 90th-percentile and standard deviation of TI

The 90th-percentile of the distribution of σ_u, $\sigma_{u,90}$, at a given wind speed is a concept relevant for turbine design. The standard deviation of σ_u, σ_{TI}, at a given wind speed corresponds to approximately 84.1^{th}-percentile.

In the IEC standard, $\sigma_{90,IEC} = 1.84 \cdot I_{ref}$ is recommended to be the 90th-percentile in relation to the mean value. I_{ref} is the reference TI at wind speed of 15 ms^{-1}, which is 0.18, 0.16, 0.14 and 0.12 for turbine type A+, A, B and C, respectively.

Wang et al. (2014) proposed the following expression to be the 90th-percentile:

$$\sigma_{u,90,W} = 0.0123 \cdot U + 0.1221, \tag{20}$$

which suggests a narrower spread of TI at higher wind speed because $\sigma_{u,90}/U = 0.0123 + 0.1221/U$.

Wang et al. (2014) also proposed an expression for σ_{σ_u}:

$$\sigma_{\sigma_u,W} = 0.0108 \cdot U + 0.1189, \tag{21}$$

whose magnitude is slightly smaller than σ_{90}.

Based on measurements from FINO 1, 2 and 3 masts, Christakos et al. (2016) derived the following expression for the standard deviation of TI varying with wind speed:

$$\sigma_{TI,C} = C_1 + C_2 \cdot e^{-C_3 U}. \tag{22}$$

They have provided detailed coefficients C_1, C_2 and C_3, depending on the site (FINO 1, 2 or 3) and height. The difference between sites and height is minor, compared to the natural spread of TI from measurements. The estimate of σ_{TI} from Christakos et al. (2016) is even larger than σ_{90} from Wang et al. (2014), suggesting the site-dependence characteristics of these empirical expressions.

We found with measurements from FINO1, 2 and 3, that the difference using the above algorithms for σ_{90} and σ_{TI} is small compared with the scatter in the measurements. Both Eq. 20 and Eq. 22 are suitable for adding variation to TI at given wind speed.

2.5 Adding the height dependence of turbulence variance

Several equations mentioned in Section Introduction implemented the height dependence of TI. Measurements from tall masts FINO 1, 2 and 3 suggest an average and approximate linear decrease of TI with height up to 100 m, see colored dots and circles in Fig. 2a. Information beyond 100 m can be partially obtained from remote sensing technique e.g., sounding or lidar measurements. Stull (1988) provided the following height dependence of wind variances:

$$\frac{\sigma_u^2}{u_*^2} = 6\left(1 - \frac{z}{z_i}\right)^2 + \frac{z}{z_i}\frac{\overline{u'^2_{top}}}{u_*^2}, \tag{23}$$

where $\overline{u'^2_{top}}$ is the variance at the top of the boundary-layer. Stull (1988) noted "Although this ratio $(\overline{u'^2_{top}}/u_*^2)$ is expected to vary from situation to situation, during the KONTUR experiment (Grant, 1986) it was found to equal 2.0...". To show Eq. 23 in the figure, we need to specify a number of variables. If we only show normalized variance $\sigma_u(z)$ by the values at 10 m, then we only need to specify z_i. Assumptions need to be made to estimate z_i and here we use the expression for neutral atmospheric boundary layer $z_i = 0.3 u_*/f_c$, with f_c the Coriolis parameter. In Fig. 2b, we plot $\sigma_u(z)/\sigma_u(10m)$ for both $u_* = 0.1$ and 0.2 ms^{-1}, to show the sensitivity.

Högström et al. (2002) provided the following theoretical expression for the height dependence of variance σ_u^2, which was validated with measurements down to a couple of meters above the ground:

$$\frac{\sigma_u^2}{u_*^2} = 2.5 + \ln\left(\frac{0.46 u_* A \kappa}{z f_c}\right), \tag{24}$$

where A can be determined through $A = f_c \frac{U}{u_*} \frac{1}{n_l}$, n_l is the lower frequency limit of the surface eddy range in Hz. In Fig. 2b, we plot $\sigma_u(z)/\sigma_u(10m)$ for both $u_* = 0.1$ and 0.2 ms^{-1}, as well as $A = 0.5$ and 0.3, to show the sensitivity.

Over water, the height dependence of the power spectrum is rather simple for the 2D turbulence as the coefficients in Eq. 8 are invariant with height at normal measurement heights, following the analysis of the measurements at Horns Rev in Larsén et al. (2016). However, the height dependence of the 3D turbulence could be complicated. The Kaimal model provides a simple

dependence of the power spectrum on z, however, its validity still needs to be verified with measurements in different ranges of wind speed and stability, as well as for heights above the surface layer. Thus, using the Kaimal model directly together with the 2D turbulence can sometimes generate a height dependence deviating significantly from the measurements and from theoretical relations that are based on measurements, e.g., those in Fig. 2b. To solve this problem, we define a coefficient α in Eq. 9 which is a function of both wind speed and height, for $z \geq 50$ m, to multiply Eq. 7, so that our LUT results are consistent with theoretical relations based on measurements at FINO 1. Appendix B provides a list of expressions of α for different wind speed ranges and different heights used for creating the LUT data.

The variances of wind speed, and TI at heights 10 m, 50 m, 100 m, 150 m and 200 m are obtained using the LUT. To compare with measurements from the three FINO masts, TI from LUT is organized for three wind speed ranges, $1-30$ m s^{-1}, $1-33$ m s^{-1} and $1-37$ m s^{-1}, which represent wind speed ranges in the three FINO sites. The TI values at z are normalized by those at 30 m (the approximate lowest measurement height at the FINO masts) and are shown in Fig. 2a (black curves). The height dependence from the ISO and its extended form, $(z/10)^{-0.22}$, is also shown in similar manner in the same figure (blue curve). Due to different measurement periods, data coverage and meteorological conditions at the three sites, there are some differences between the results from the three sites. Nevertheless, the agreement is striking between them, and there is an overall good agreement between the measurements and the LUT data. The ISO and its extended expressions, with $(z/10)^{-0.22}$ corresponds to a much stronger decrease of TI with height, particularly in the lowest 100 m, when compared with measurements. At higher elevations, it is approaching similar decreasing rate with height to the LUT results.

Similar trend between the four data sources is observed in Fig. 2b, where the vertical distribution of the wind speed variance, normalized by the value at 10 m, $\sigma_u(z)/\sigma_u(10m)$, is shown. As introduced before, both $u_* = 0.1$ and 0.2 ms^{-1} are used, and for Eq. 24, $A = 0.3$ and 0.5 are used, to show the variation in connection with the use of the two expressions. In general, higher z_i (corresponding to larger u_* and A) results in a slower decrease with height. For the comparison, to match the general wind conditions from Stull (1988) and Högström et al. (2002), we extracted the variance from the LUT data for wind speed at 10 m not exceeding 18 ms^{-1}. The ISO expression of the height-dependence does not distinguish between wind speed ranges, and consistent with Fig. 2a, it provides the strongest decrease with height for $z < 100$ m.

3 Data

3.1 The base model data

In this study, we use ERA5 data (Hersbach et al., 2020) to demonstrate the calculation of global offshore turbulence intensity using the algorithms presented in Section 2. ERA5 is chosen because of the global availability of both atmospheric and wave data. Other atmospheric and wave data can also be used.

In order to match the Global Wind Atlas data layers, including both resource and site parameters (Larsén et al., 2021; Davis et al., 2023), the ERA5 reanalysis from the same period 2008–2017 (both years included) was used here. ERA5 data are available with an hourly time-resolution. The meteorological data (wind speed components, 2-m temperature, friction velocity) are available with horizontal spatial grid spacing of $0.25° \times 0.25°$ (about 30 km in the mid-latitude), and the ocean wave data
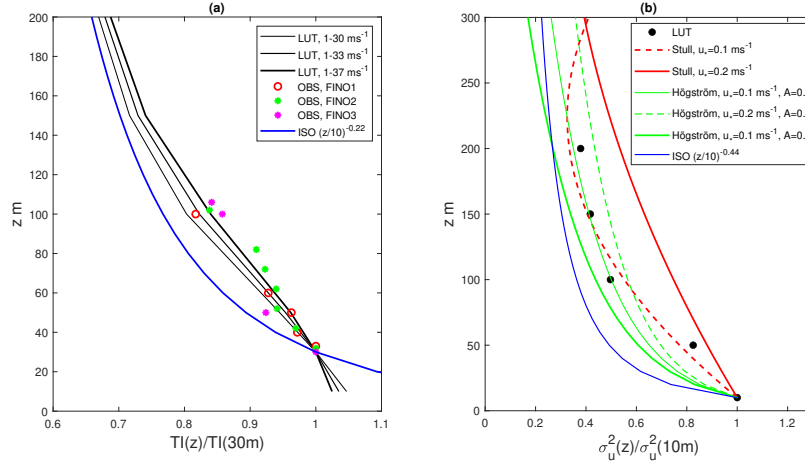
Figure 2. (a) TI normalized with TI at 30 m, with data from measurements at the three FINO sites, ISO expression and LUT method. (b) Comparison of the distribution of wind speed variance with height, normalized with value at 10 m, following the theoretical expressions of Stull (1988) and Högström et al. (2002)

is only available on a $0.5° \times 0.5°$ spatial grid. To avoid unnecessary interpolation of the wave data, our analysis is performed on the wave data grids only.

The following time series from the ERA5 data have been used: meridional and longitudinal wind components at 10 m (U_{10m}, V_{10m}), wave period at peak frequency (T_p), temperature at 2 m T_{2m}, meridional and longitudinal stress components $\overline{U'w'}$ and

260    $\overline{V'w'}$, and surface heat flux $\overline{w'\theta'}$. We also used static bathymetry data.

From the above data, the following variables are derived for 12 directional sectors for all water model grids: (1) mean wind speed at 10 m from the meridional and longitudinal components; (2) frequency of occurrence; (3) mean friction velocity $u_* = (\overline{U'w'}^2 + \overline{V'w'}^2)^{1/4}$; (4) mean temperature scale ($\overline{w'\theta'}/u_*$), and hence Obukhov length (L); (5) mean wave phase velocity (c_p) with water depth (h) effect considered through Eq. 14.

265   **3.2   Validation data**

In this study, we use 10-min time series of wind speed and standard deviation from FINO 1, 2 and 3 at heights from 30 to about 100 m, to examine the calculation of TI, 90th-percentile and standard deviation of TI, as well as the dependence of TI on height z.

Some other measurements are not open source like the FINO data, so we use the published analysis based on these measure-

270   ments for comparison, here including results based on

- 11 offshore sites from Jeans (2024), showing the dependence of TI on U at different heights

- Horns Rev site from Wang et al. (2004), showing the dependence of TI on U at 50 m

– Høvsøre from Peña et al. (2016), showing the dependence of TI on U at 100 m

4 Results

275 ### 4.1 The Look-Up Table for TI

Using the algorithms presented in Section 2, a Look-Up Table, LUT, is generated where TI is a function of wind speed U, height z, wave phase velocity c_p and stability z/L at 10 m. Figure 3 shows an example of some distributions of TI from the LUT at 10 m. Neutral stability has been applied in Fig. 3a to c, and the stability effect is added in Fig. 3d.

The focus of Fig. 3a is to show the effect of waves on TI. To demonstrate this, we first calculate TI excluding the depen-
280 dence of wave age on α_{ch} and using $\alpha_{ch} = 0.011$ instead. The result is shown in the dashed blue curve. At the same time, we also use the drag coefficient description from the Spectral WAve Nearshore (SWAN) model $C_D = (0.55 + 2.97(U_{10}/31.5 - 1.49(U_{10}/31.5)^2) \times 10^{-3}$ (Zijlema et al., 2012). This expression allows a simple dependence of surface stress on 10 m wind speed, and through the logarithmic wind law Eq. 18, converts to z_0. Consequently, TI increases with wind speed up to about 18 m s^{-1}, very close to the expression of Charnock with $\alpha_{ch} = 0.011$, and the increase slows down and becomes a decreasing
285 dependence on wind speed for winds stronger than 31.5 m s^{-1}, in contrast to Charnock with $\alpha_{ch} = 0.011$. The SWAN expression was derived from measurements collected in various stations and different weather conditions. The decrease of C_D and TI for $U_{10m} > 31$ ms^{-1} was considered to be associated with wave breaking processes.

In comparison, results from LUT using Eq. 12 in the black dots in Fig. 3a show the variation in TI at a given wind speed, caused by including the wave age effect through c_p/u_*. At a given wind speed, the younger the waves, the smaller their age
290 c_p/u_*, the larger TI. The spread in TI is larger at stronger winds. At $U_{10} = 15$ ms^{-1}, the difference caused by c_p/u_* in TI is on the order of 0.01. There is a weak decrease of TI with U in light winds due to the smooth flow effect, followed by an increase in TI with U up to approximately 31 ms^{-1}. As can be seen in Fig. 3a, for winds stronger than 31 ms^{-1}, for the youngest waves, TI continues to increase with U, but at a lower rate; most often, TI decreases with U again, as Eq. 13 incorporates a simplified description of the wave-breaking process in the strongest winds.

295 Figure 3a shows the calculation using only 3D turbulence (Eq. 7), while from Fig. 3a to b, 2D turbulence is added to the calculation of variance, and hence TI. The effect of including the 2D turbulence is shown in Fig. 3c in red dots; the black dots are the same as in Fig. 3a. Comparison of the black with the red dots in Fig. 3c suggests that the effect of including 2D turbulence is most obvious at light to medium wind speeds, where TI decreases from much higher values with U up to about 7 ms^{-1}. Measurements have consistently shown these high values of TI in low to moderate winds, e.g., in Wang et al.
300 (2014),Peña et al. (2016),Christakos et al. (2016) and Jeans (2024).

Based on the values in Fig. 3c, TI is calculated by using Eq. 19 with z/L varying from -3 (highest curve) to 3 (lowest curve). Figure 3d shows an example of the impact of stability at a given $c_p = 10$ m s^{-1}.

Corresponding data and LUTs are also made available at 50 m, 100 m, 150 m and 200 m. Values at heights in between can be interpolated.
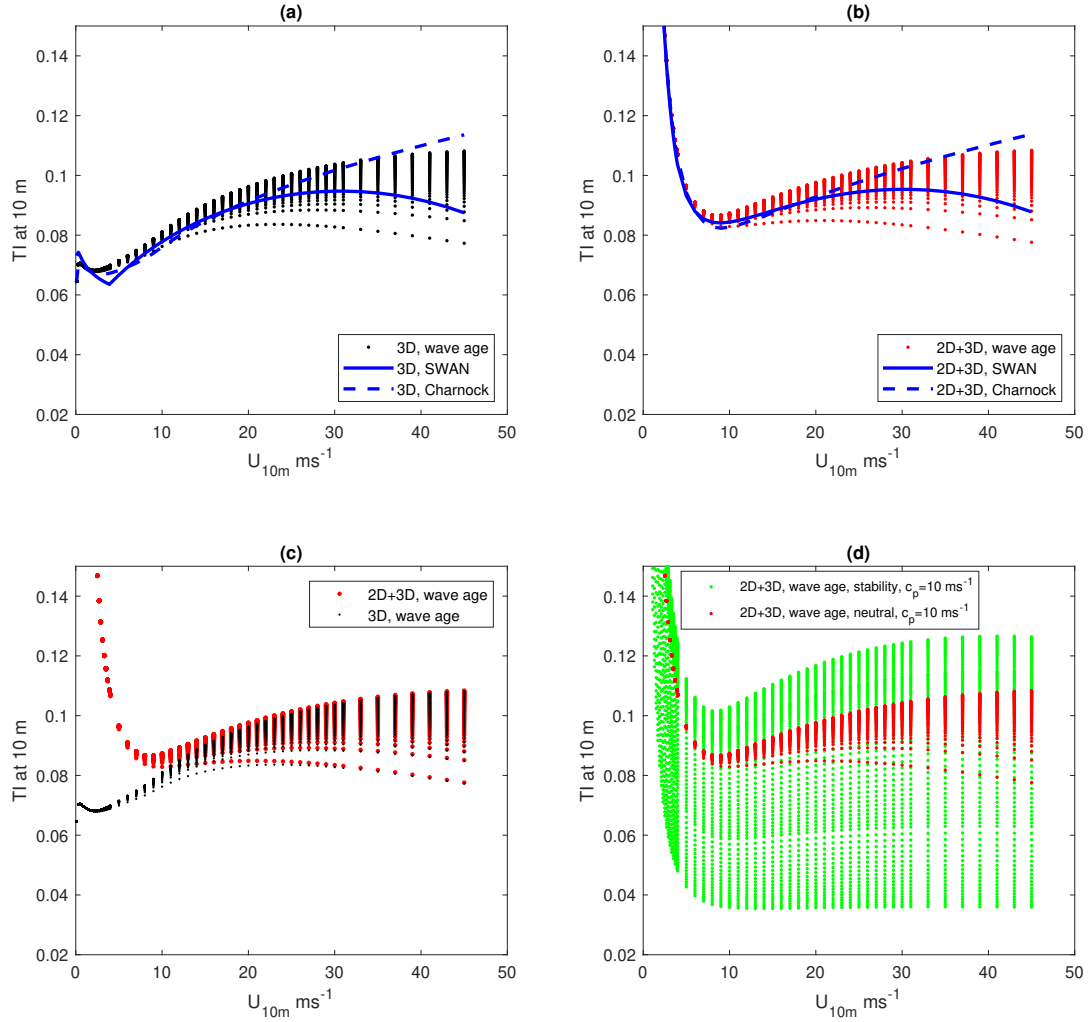
Figure 3. An example of the distribution of the turbulence intensity (TI) with wind speed at 10 m. (a) includes only microscale (3D) turbulence, and shows difference of including wave-age dependence, using $z_0 = 0.011 u_*/g$ (dashed curve), and using the SWAN algorithm (solid curve). (b) is similar to (a), but including the large-scale (2D) turbulence. (c) shows the difference between including and excluding the 2D turbulence in the calculation of TI. (d) The red dots are the same as from (b) and (c) showing the effect of wave age and 2D turbulence, but for neutral conditions. The green dots in (d) shows the effect of stability from $z/L = -3$ to 3, for the group where $c_p = 10$ ms^{-1}.
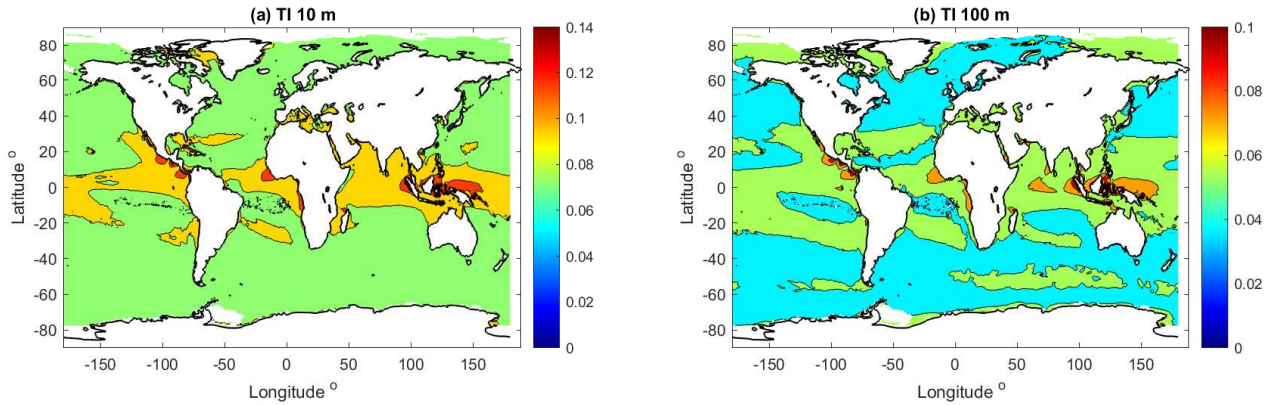
Figure 4. Global atlases of the mean turbulence intensity at (a) 10 m and (b) 100 m for offshore grid points, including 2D turbulence, wave age and stability effect.

4.2 The global offshore atlas of turbulence intensity

For a given offshore location, if we can get basic information on z/L and c_p, we can use the LUT and identify TI as a function of the wind speed at 5 heights $z =$10, 50, 100, 150 and 200 m. In the absence of certain information, one can always assume neutral stability, skip the wave-age dependence, and use e.g., the SWAN expression (e.g., the blue curve in Fig. 3b).

With additional information on the wind speed frequency distribution as a function of each wind condition, we can calculate the corresponding TI distribution at the site. The frequency of occurrence can also be used to weight the calculation in obtaining the mean values of TI.

The information about stability, waves and wind speed distribution can be obtained either from measurements or from modeling. We have prepared global data for these variables based on the ERA5 data. Here we prepared mean values of z/L, c_p and wind speed in 12 sectors and their occurrence frequencies.

Figure 4a and b show an example of the global distribution of offshore, mean values of TI at ERA5 grid points at 10 and 100 m respectively.

4.3 Validation at sites

4.3.1 $TI - U$ distribution

First, we compare our calculation with the results from Jeans (2024) at 11 offshore stations. We extracted data from their Fig. 5 for these sites and plotted them here in Fig. 5, including measurements (red dots) and their calculation using Eq. 4 (blue, dashed curves). The site names and data heights are shown in the subplots' labels.

With the given locations of these 11 sites from that study, we extracted the corresponding data from the ERA5 derived atlas as shown in section 4.2, including z/L, c_p, wind speed and occurrence frequency in 12 sectors. These data were used to identify the corresponding TI from the LUT.

Three of the 11 sites, Frøya Sletringen, Frøya Skipheia and Egmond aan Zee, correspond to ERA5 land grid points as there are small islands nearby. We used the neighboring water grid point to represent each of the three sites.

To obtain the LUT results at the corresponding heights for the 11 sites as in Fig.s 5 and 6 in Jeans (2024), we used the data at two neighboring heights and applied linear interpolation. The results are shown in black, solid curves in Fig. 5. Our calculation shows good agreement with both measurements and Jeans' calculation using Eq. 4. Our calculation in general improves TI at stronger winds. There is improvement with the LUT method in comparison with those in Jeans (2024) for Fig. 5a, b, c, d, e and f, particularly for moderate to strong winds. For wind speed stronger than 8 m s^{-1}, the mean absolute error (MAE) for TI is 0.0031 for LUT, and 0.0042 for Jeans (2024), and the corresponding MAE are 0.0029 and 0.0043 for wind speed stronger than 15 m s^{-1}. Such an improvement of using the LUT method is also visible for two additional sites, Høvsøre and Horns Rev, shown in Fig. 6a and b, respectively. Here TI as a function of U from measurements are extracted from the studies of Peña et al. (2016) and Wang et al. (2014), respectively.

4.3.2 90th-percentile of TI

Using the mean values of wind, wave parameter and stability in 12 sectors derived from ERA5 data as input to the LUT method does not provide a representative scatter of TI. The LUT method here adopts the algorithms from the literature for describing the 90th-percentile and the standard deviation of TI. Figure 7 shows an example for the site FINO 1. The mean and 90th-percentile of TI at wind speed bins are calculated from measurements, from IEC standard and from the algorithm provided by Wang et al. (2014). In addition, we also calculated σ_{TI} at these wind speed bins using the algorithm of Christakos et al. (2016) through measurements from FINO sites. Both the algorithms from Wang et al. (2014) and Christakos et al. (2016) can reasonably well describe the 90th-percentile of TI from the measurements here.

5 Discussion

This study provides a method as well as an example database for turbulence intensity for offshore conditions globally, from 10 m to 200 m, which are heights relevant for existing turbine types. The data include sectorwise distributions of mean as well as standard deviation of TI as a function of wind speed from calm to gale wind conditions.

From this method, a Look-Up Table (LUT) is created, where TI can be identified with input of wind speed (U_z), stability (z/L at 10 m), wave phase velocity (c_p), and height (z). The interface for input (U_z, z/L, c_p and z) allows the use of data from any source for preparing these variables. It could be from measurements, modeled data, or combined.

We used the modeled data for demonstration of the use of the LUT, here through ERA5 data, from which U_z, z/L, c_p and z can easily be prepared. One could also use e.g., the New European Wind Atlas (NEWA) data (Dörenkämper et al., 2020) for preparing atmospheric parameters U_z,z/L, and z, and use another source for wave parameter c_p. This would of course bring
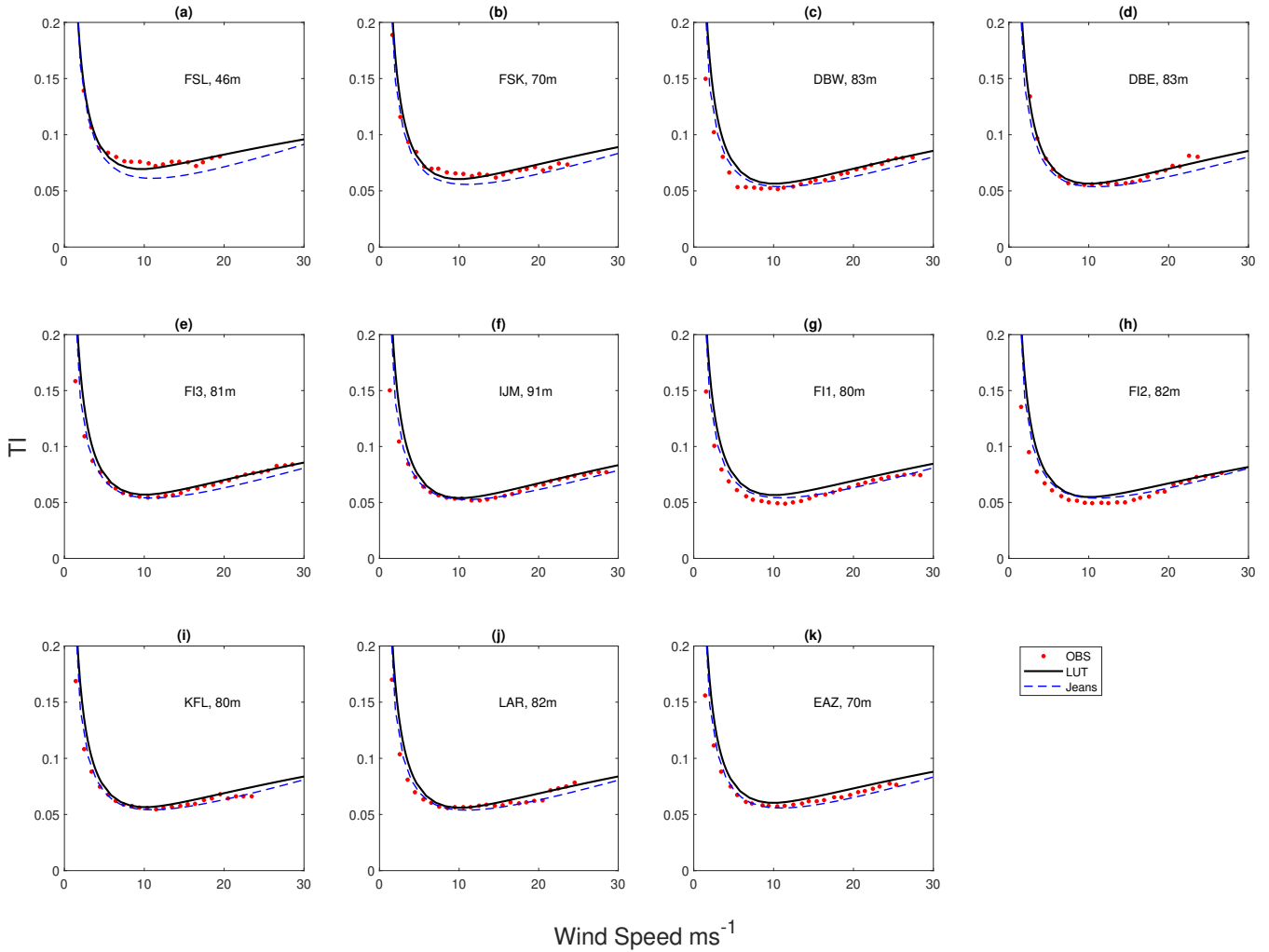
Figure 5. Comparison of TI from the LUT method (black curves) with values from measurements (red dots) and Eq. 4 from Jeans (2024) (blue dashed). The measurements are extracted from Jeans (2024). The names of the sites are: (a) Frøya Sletringen, (b) Frøya Skipheia, (c) Dogger Bank West, (d) Dogger Bank East, (e) FINO3, (f) IJmuiden, (g) FINO1, (h) FINO2, (i) Kentish Flats, (j) London Array and (k) Egmond aan Zee, and the corresponding heights of measurements used in the plot are shown in the subplots.
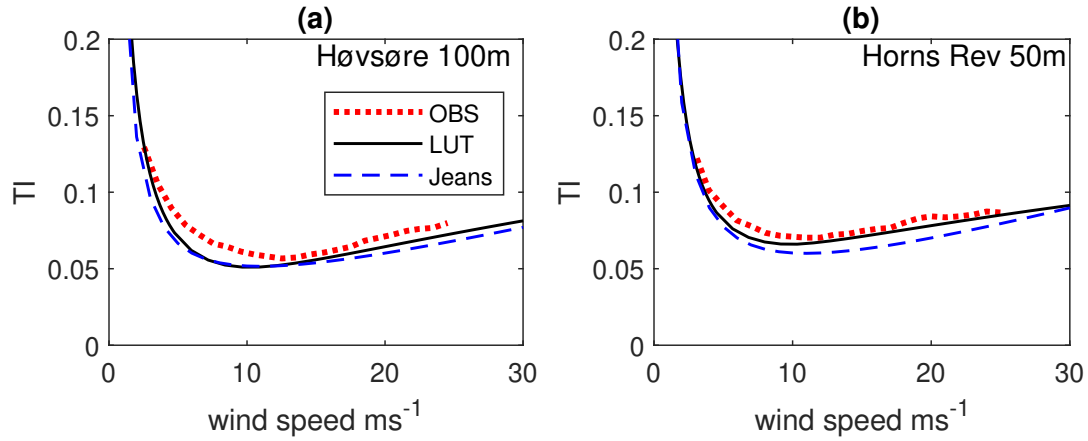
Figure 6. Comparison of TI from the LUT method (black curves) with values from published measurements (red dots) at two sites Høvsøre (Peña et al., 2016) and Horns Rev (Wang et al., 2014), and Eq. 4 from Jeans (2024) (blue dashed).

additional uncertainty due to inconsistency in data sources. Nevertheless it is worth trying and being validated for individual

355 cases, as a complete set of both atmospheric and wave data is not easy to obtain. If the wave data are absent or proven to be unreliable, one could also neglect the wave age dependence in the calculation. This corresponds to using the blue solid curve in Fig. 3b, instead of the red dots.

The ERA5 data has a global coverage including both atmospheric and wave data, but are of relatively coarse spatial resolution. This leads to higher uncertainties in coastal zones where the detailed spatial features are not resolved. However, in

360 the LUT method calculations, the ERA5 data can be straightforwardly replaced by other model data with a higher spatial resolution, when possible.

The LUT method is based on physical principles and it implements algorithms that have been derived from theory and measurements, and validated with measurements.

The LUT method includes atmospheric stability effect through Monin-Obukhov similarity theory. ERA5 surface fluxes are

365 used to calculate the Obukhov length L, which is afterwards used to convert TI from neutral conditions to the corresponding stability conditions. All the 13 validation sites are in the North Sea region; the combined data show that there is a dependence of mean values of z/L on the sectors, with the majority of the data in the range $-0.1 < z/L < 0$ in most sectors and $0 < z/L < 0.05$ in southwest sectors. In general, the averaged stability effect is not significant at the sites shown here, at least from the ERA5 data, but it may be important at other locations.

370 The LUT method uses the Fan scheme (Fan et al., 2016) for the roughness length z_0, which is a function of wave age c_p/u_* and wind speed. The use of the Fan scheme successfully describes the increasing dependence of TI on wind speed for moderate to strong winds, here validated with measurements up to about 30 ms^{-1}. Note that like most parameterization schemes for z_0, wave conditions are simplified using the Fan scheme, here Eqs 11 to 14. For instance, the fetch effect on the wave field is not considered. Only the most dominant wave with a peak frequency is considered when c_p is used. At the same time, in connection
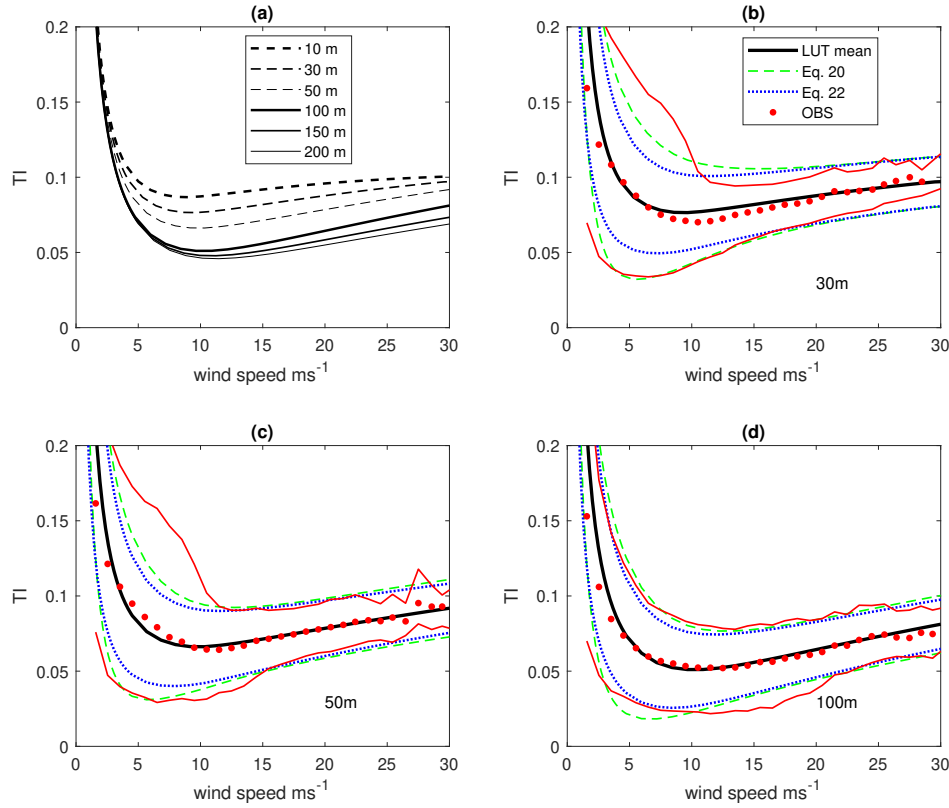
Figure 7. Presentation of TI from the LUT method at FINO 1. (a) Mean values of TI varying with wind speed at 6 heights from 10 m to 200 m. (b) FINO 1, at 30 m, showing mean TI (measurements and LUT), 90th-percentile of TI from measurements (red curve), and derived from Eq. 20 (dashed green curve) and σ_{TI} (Eq. 22, dotted blue curve).

with the use of the global ERA5 wave data, the wave parameters are only available every 50 km approximately for the sites we studied here. This implies that most of the ERA5 data are quite far from the coastlines and are likely more representative for open ocean conditions. At the 13 validation sites, the average c_p/u_* is 33 with a standard deviation 11, and the minimum and maximum are 15 and 79, respectively.

Two major contributions from the LUT method are particularly worth highlighting, in comparison with previous studies.

The first is the inclusion of the large-scale, two-dimensional turbulence, which results in the decreasing dependence of TI with wind speed for lower wind speed ranges. Previously, this part was taken care of by imposing an empirical and artificial dependence, e.g. ($z^{-0.22}$), or an assumption of climatological unstable conditions at low wind speed (Wang et al., 2014). The observed large values of TI at light winds are often associated with convective conditions. Even though we included the stability effect through $\psi(z/L)$ as in Eq. 19, this effect through the ERA5 data is not obvious as expected. Note that we did not include the stability effect in the derivation through the turbulence spectrum, which is used to calculate σ_U in $TI_N = \sigma_U/U_N$. Figure 3c shows that the most significant effect from the 2D turbulence on TI is for light to medium wind speeds. At strong

winds, the surface driven turbulence that is generated using e.g. the Kaimal spectral model under neutral condition, is significant in comparison with the 2D turbulence. At weak winds, the calculated 2D turbulence becomes relatively more important as the Kaimal model generates relatively little turbulence. Inclusion of large-scale wind variability through the 2D turbulence model

390 for weak to medium wind speeds thus compensates the lack of consideration of stability in the 3D spectrum. As a result, more realistic level of total turbulence calculation is obtained.

The second is the systematic calibration of height dependence of the calculation of TI up to 200 m with historic measurements-based studies and measurements from FINO 1. The outcome is satisfactory at validation sites (Fig. 2a, Fig. 5 to Fig. 7). The height dependence such as in the ISO standard ($z^{-0.22}$) seems to be too strong in the lowest 200 m, see Fig. 2a and b. Note that

395 the validation of TI in (Jeans, 2024) is done mostly at one height.

For a global calculation, using a look-up table simplifies the calculation significantly and saves computation. The mean statistics of $TI - U$ relationships and its dependence with height is well captured by the LUT method. To handle the large global ERA5 dataset, only the mean values from 12 directional sectors are stored for wind speed, c_p and L. The spread of TI, associated with wind, stability, wave, fetch, as well as their sectorwise dependence, is thus underestimated by using

400 the sectorwise mean values of the ERA5 data. A simple solution is taken here preliminarily through the use of the existing algorithms for describing the standard deviation of TI, or the 90th-percentile.

In the future, other data with higher resolution than the ERA5 data can be used to provide the input to apply the LUT method. One could also include more advanced statistics than the sectorwise mean values as input to the LUT method, thus improving the calculation of the spread of TI.

405 ## 6 Conclusions

This study delivers the Look-Up Table (LUT) method for the turbulence intensity (TI) of offshore conditions. The method describes TI through both the two and three-dimensional turbulence, making it suitable for heights above the atmospheric surface layer. At weak wind conditions, this systematically includes the effect of large eddies through the two-dimensional turbulence, which otherwise is neglected in using the three-dimensional turbulence only under the assumption of neutral stability

410 and weak wind. Accordingly, it captures the decreasing dependence of TI for light to moderate winds. This method describes the roughness length z_0 through dependence on wind speed and wave age, which accurately describes TI for moderate to strong winds, including wave breaking effect. Stability effect is also included. The method for TI can be applied globally and was calibrated to a height of 200 m.

The global data prepared using this method together with the global ERA5 wind and wave data was shown to perform

415 reasonably well with validations from 13 offshore sites and comparison with earlier studies. With a given location, we can find the corresponding ERA5 coordinates, and extract the corresponding data. The LUT will then provide TI according to these information at the above mentioned 5 heights. If the height of interest is in between those five heights, one can interpolate between neighboring heights.

This method is flexible to use, if one has special data as input. In the absence of other data sources, one can use the global
420   ERA5 data prepared here by providing the coordinate for the site of interest.

Data availability.   Data and codes are published at https://data.dtu.dk/account/articles/30575555

.

Appendix A: Collection of expressions of TI

The detailed expressions for TI from Wang et al. (2014) and Andersen and Løvseth (2006) are provided here. Specifically, the
425   equation of TI from Wang et al. (2014) reads:

$$TI_{Wang} = \frac{\kappa(C_{NT}^2 + C_{mX}^2(-z_i/L)^{2/3})^{1/2}}{\ln z/z_0 - \psi_m(z/L)} \tag{A1}$$

where C_{NT} and C_{MX} are two constants as approximates for σ/u_* and σ/w_*, respectively. for neutral and mixed-layer conditions, u_* is the friction velocity and w_* is the convective velocity scale and it is a function of temperature, surface heat flux and height of the boundary layer z_i, and L is the Obukhov Length.

430   There are several similar expressions in Andersen and Løvseth (2006), primarily for the wind speed range from 10 to 26 ms^{-1}, including the "modified Vickery model":

$$TI_{Vic} = 0.085(\frac{U}{10})^{0.421}(\frac{z}{10})^{-0.2}, \tag{A2}$$

the "drag coefficient model":

$$TI_{Dra} = 0.0857(1 + 0.758(\frac{U}{10} - 1))^{0.5}(\frac{z}{10})^{-0.2}, \tag{A3}$$

435   and the "linear model":

$$TI_{Lin} = 0.087(1 + 0.302(\frac{U}{10} - 1))(\frac{z}{10})^{-0.2}. \tag{A4}$$

The above three expressions, Eq. A2 to A4, provide similar estimates up to wind speed of 26 ms^{-1}, which describe well the measurements at the Frøya site from 10 m to 46 m. Above 26 ms^{-1}, there are no measurements and the linear model gives considerably larger values, which was recommended by the authors for slightly conservative design approach.

440   ## Appendix B: Calculating the height dependence of variance

In the process of calibration using measurements from FINO 1, we added a coefficient α to the Kaimal model expression for u for z from 50 m and above. The coefficient α is a function of wind speed at each height.

$$\alpha_{50m} = 0.018U + 0.54, \quad U \le 10 \; ms^{-1} \tag{B1}$$
$$= 0.024U + 0.48, \quad 10 < U \le 32 \; ms^{-1} \tag{B2}$$
$$= 1.29, \quad U > 32 \; ms^{-1} \tag{B3}$$

$$\alpha_{100m} = 0.035U + 0.037, \quad U \le 35 \; ms^{-1} \tag{B4}$$
$$= 1.26, \quad U > 35 \; ms^{-1} \tag{B5}$$

$$\alpha_{150m} = 0.031U + 0.033, \quad U \le 35 \; ms^{-1} \tag{B6}$$
$$= 1.12, \quad U > 35 \; ms^{-1} \tag{B7}$$

$$\alpha_{200m} = 0.029U + 0.031, \quad U \le 35 \; ms^{-1} \tag{B8}$$
$$= 1.05, \quad U > 35 \; ms^{-1} \tag{B9}$$

Author contributions. XL designed the study, developed the method, did the calculation of TI, outlined and wrote the paper. MI contributed with preparation of global ERA5 data for the wind and wave statistics, and to editing the paper. RF contributed with the prepartion of global ERA5 data for the stability parameters, and to editing the paper.

Competing interests. The authors declare that they have no conflict of interest.

Acknowledgements. This study is supported by the Danish EUDP GASPOC J. nr. (65020-1043), EUDP IDEA project (134-21029) and Horizon Europe project DTWO (101146689)

References

Andersen, O. J. and Løvseth, J.: The Frøya database and matitime boundary layer wind description, Marine Structures, https://doi.org/10.1016/j.marstruc.2006.07.003, 2006.

Andreas, E. L., Mahrt, L., and Vickers, D.: An improved bulk air-sea surface flux algorithm, including spray-mediated transfer, Q.J.R. Meteorol. Soc., 141, 642–654, https://doi.org/10.1002/qj.2424, 2015.

Christakos, K., Mathiesen, M., Henrik, O., Holvik, S., and Meyer, A.: Turbulence Intensity Model for Offshore Wind Energy Applications, https://www.sintef.no/globalassets/project/eera-deepwind2016/presentations/c1$_christakos_metoceanconditions.pdf$/, 2016.

Davis, N. N., Badger, J., Hahmann, A. N., Hansen, B. O., Mortensen, N. G., Kelly, M., Larsén, X. G., Olsen, B. T., Floors, R., Lizcano, G., Casso, P., Lacave, O., Bosch, A., Bauwens, I., Knight, O. J., van Loon, A. P., Fox, R., Parvanyan, T., Hansen, S. B. K., Heathfield, D., Onninen, M., and Drummond, R.: The Global Wind Atlas: A High-Resolution Dataset of Climatologies and Associated Web-Based Application, Bulletin of the American Meteorological Society, 104, E1507 – E1525, https://doi.org/10.1175/BAMS-D-21-0075.1, 2023.

Dörenkämper, M., Olsen, B. T., Witha, B., Hahmann, A. N., Davis, N. N., Barcons, J., et al.: The making of the new European wind atlas–part 2: Production and evaluation, Geoscientific Model Development, 13, 5079–5102, 2020.

Fan, Y., Lin, S., Held, I., Yu, Z., and Tolman, H.: Global ocean surface wave simulation using a coupled atmosphere-wave model, J. Clim., 25, 6233–6252, 2016.

Grant, A.: Observations of boundary layer structure made during the 1981 KONTUR experiment, Royal Meteorological Society, 112, https://doi.org/10.1002/qj.49711247314, 1986.

Hersbach, H., Bell, B., Berrisford, P., Hirahara, S., Horányi, A., Muñoz-Sabater, J., Nicolas, J., Peubey, C., Radu, R., Schepers, D., Simmons, A., Soci, C., Abdalla, S., Abellan, X., Balsamo, G., Bechtold, P., Biavati, G., Bidlot, J., Bonavita, M., De Chiara, G., Dahlgren, P., Dee, D., Diamantakis, M., Dragani, R., Flemming, J., Forbes, R., Fuentes, M., Geer, A., Haimberger, L., Healy, S., Hogan, R. J., Hólm, E., Janisková, M., Keeley, S., Laloyaux, P., Lopez, P., Lupu, C., Radnoti, G., de Rosnay, P., Rozum, I., Vamborg, F., Villaume, S., and Thépaut, J.-N.: The ERA5 global reanalysis, Quarterly Journal of the Royal Meteorological Society, 146, 1999–2049, https://doi.org/https://doi.org/10.1002/qj.3803, 2020.

Högström, U.: Review of some basic characteristics of the atmospheric surface layer, Boundary-Layer Meteorology, 78, 215–246, 1996.

Högström, U., Hunt, J. C. T., and Smedman, A.: Theory and measurements for turbulence spectra and variances in the atmospheric surface layer, Boundary-Layer Meteorology, 103, 101–124, 2002.

IEC: IEC 61400-1 Ed4: Wind turbines - Part 1: Design requirements, standard, International Electrotechnical Commission, Geneva, Switzerland, 2019.

ISO: Petroleum and natural gas industries – Specific requirements for offshore structures – Part 1: Metocean design and operating considerations, www.iso.org/standard/60183.html, ISO 19901-1:2015, 2015.

Jeans, G.: Converging profile relationships for offshore wind speed and turbulence intensity, Wind Energ. Sci., https://doi.org/10.5194/wes-9-2001-2024, 2024.

Kaimal, J., Wyngaard, J., Izumi, Y., and Coté, O.: Spectral characteristics of surface-layer turbulence, Q. J. R. Meteorol. Soc, 98, 563–589, 1972.

Kosovic, B., Basu, S., Berg, J., Berg, L. K., Haupt, S. E., Larsén, X. G., Peinke, J., Stevens, R. J. A. M., Veers, P., and Watson, S.: Impact of atmospheric turbulence on performance and loads of wind turbines: Knowledge gaps and research challenges, Wind Energy Sci., https://doi.org/10.5194/wes-2025-42, 2025.

Larsén, X., Davis, N., Hannesdóttir, Á., Kelly, M., Svenningsen, L., Slot, L., Imberger, M., Olsen, B., and Floors, R.: The Global Atlas for Siting Parameters project: Extreme wind, turbulence, and turbine classes, https://doi.org/10.1002/we.2771, 2022.

495 Larsén, X. G., Larsen, S. E., and Petersen, E. L.: Full-scale spectrum of boundary-layer winds, Bound.-Layer Meteorol., 159, 349–371, 2016.

Larsén, X. G., Davis, N., Hannesdóttir, A., Kelly, M., Svenningsen, L., and Slot, R.: Global Atlas of Siting Parameters V1 Dataset, Tech. rep., Wind Energy Department, Technical University of Denmark, Roskilde, Denmark, https://doi.org/https://doi.org/10.11583/DTU.14753349, 2021.

Larsén, X. G., Vincent, C. L., and Larsen, S.: Spectral structure of the mesoscale winds over the water, Q. J. R. Meteorol. Soc., 139, 685–700,

500 https://doi.org/DOI:10.1002/qj.2003, 2013.

Larsén, X. G., Du, J., Bolanos, R., Imberger, M., Kelly, M., Badger, M., and Larsen, S. E.: Estimation of offshore extreme wind from wind-wave coupled modeling, Wind Energy, 22, 1043–1057, https://doi.org/10.1002/we.2339, 2019.

Mann, J.: The spatial structure of neutral atmospheric surface-layer turbulence, J. Fluid Mech., 273, 141–168, https://doi.org/10.1017/S0022112094001886, 1994.

505 Peña, A., Floors, R., Sathe, A., Gryning, S.-E., Wagner, R., Courtney, M., Larsén, X., Hahmann, A., and Hasager, C.: Ten Years of Boundary-Layer and Wind-Power Meteorology at Høvsøre, Denmark, Boundary-Layer Meteorology, 158, 1–26, https://doi.org/10.1007/s10546-015-0079-8, © The Author(s) 2015. This article is published with open access at Springerlink.com, 2016.

Stull, R.: An Introduction to Boundary Layer Meteorology, Springer Dordrecht, https://doi.org/10.1007/978-94-009-3027-8, 1988.

Tai, S.-L., Berg, L. K., Krishnamurthy, R., Newsom, R., and Kirincich, A.: Validation of turbulence intensity as simulated by the Weather

510 Research and Forecasting model off the US northeast coast, Wind Energy Science, 8, 433–448, https://doi.org/10.5194/wes-8-433-2023, 2023.

Veers, P.: Three-Dimensional Wind Simulation, SANDIA REPORT, 1988.

Wang, H., Barthelmie, R. J., Pryor, S. C., and Kim, H. G.: A new turbulence model for offshore wind turbine standards, Wind Energy, https://doi.org/10.1002/we.1654, 2014.

515 Zijlema, M., Van Vledder, G., and Holthuijsen, L.: Bottom friction and wind drag for wave models, Coast Eng, 65, 19–26, 2012.